A&A 472, 727–737 (2007)
DOI: 10.1051/0004-6361:20077466

Astronomy & Astrophysics

High redshift X-ray galaxy clusters

I. The impact of point sources on the cluster properties⋆

M. Branchesi[1,2], I. M. Gioia[2], C. Fanti[2], and R. Fanti[2]

[1] Dipartimento di Astronomia, Università di Bologna, via Ranzani 1, 40127 Bologna, Italy
e-mail: m.branchesi@ira.inaf.it
[2] INAF – Istituto di Radioastronomia, via Gobetti 101, 40129 Bologna, Italy
e-mail: [gioia;rfanti;cfanti]@ira.inaf.it

Received 13 March 2007 / Accepted 17 June 2007

ABSTRACT

Context. The current generation of X-ray observatories like *Chandra* allows studies with very fine spatial details. It is now possible to resolve X-ray point sources projected into the cluster diffuse emission and exclude them from the analysis to estimate the "correct" X-ray observables.
Aims. We wish to verify the incidence of point sources on the cluster thermal emission and to evaluate the impact of their non-thermal emission on the determination of cluster properties.
Methods. To these ends we use a sample of 18 high-z ($0.25 < z < 1.01$) clusters from the *Chandra* archive and subtract the non-thermal emission of the point sources from the extended thermal emission due to the cluster itself. We perform a detailed analysis of the cluster properties and compare the changes observed in the X-ray observables, like temperature and luminosity or their inter-relation, when one keeps the point sources in the analysis.
Results. The point sources projected into the cluster extended emission affect the estimates of cluster temperature or luminosity considerably (up to 13% and 17% respectively). These percentages become even larger for clusters with $z > 0.7$ where temperature and luminosity increase up to 24% and 22%, respectively.
Conclusions. The conclusions are that point sources should be removed to correctly estimate the cluster properties. However the inclusion of the point sources does not impact significantly the slope and normalization of the $L_{\rm bol}$–T relationship since for each cluster the correction to be applied to T and $L_{\rm bol}$ produces a moderate shift in the $L_{\rm bol}$–T plane almost parallel to the best-fit of the "correct" $L_{\rm bol}$–T relation.

Key words. galaxies: clusters: general – galaxies: high-redshift – cosmology: observations – galaxies: intergalactic medium – X-rays: galaxies: clusters

1. Introduction

X-ray studies of clusters of galaxies performed with X-ray telescopes like *ASCA* (Tanaka et al. 1994), *Beppo-SAX* (Parmar et al. 1997; Manzo et al. 1997; Boella et al. 1997; Frontera et al. 1997) or *ROSAT* (Trümper 1984) have attributed the total X-ray emission from clusters of galaxies to thermal bremsstrahlung emission from the thin hot gas that fills the regions between the cluster galaxies. This is due to the optimal consistence between the observed X-ray spectra and the expected thermal emission from the highly ionized hydrogen and helium in the intra-cluster medium at temperatures $T \sim 10^7$–1.5×10^8 K. The detection of point sources in the cluster fields has been hindered by the traditionally poor angular resolution of such X-ray telescopes. The current generation of X-ray observatories like *Chandra* (van Speybroeck et al. 1997) or XMM-*Newton* (Strüder et al. 2001; Turner et al. 2001) has revolutionized X-ray astronomy, enabling studies with very fine spatial details. In addition the improvement of detection techniques (e.g. the multiscale wavelet detection by Freeman et al. 2002) can now reliably separate small-scale source emission from surrounding larger-scale diffuse cluster emission. Hence, it is now possible to subtract the non-thermal emission of the point sources embedded in the cluster emission from the extended thermal emission due to the cluster itself. In recent years a number of detailed XMM-*Newton* and *Chandra* studies have allowed investigators to compute the "correct X-ray observables" and thus the "correct scaling relations" between them excluding the point sources from the analysis of the cluster emission.

In this paper we present a detailed analysis of the archival *Chandra* data for a sample of high-z clusters. The aim is to verify the incidence of point sources on the thermal emission of the cluster and to evaluate their contribution to the cluster total emission. In particular we will examine the point source effects on the cluster temperature and luminosity and on the $L_{\rm X}$–T relation. The sample analyzed consists of eighteen clusters with redshift in the range $0.25 < z < 1.01$, that was also used by Branchesi et al. (2007a) (from now on BR07) to check for any overdensity of point sources in the inner region of clusters of galaxies. In a companion paper (Branchesi et al. 2007b, Paper II) we will use these same clusters in combination with clusters taken from the literature to revisit the "correct $L_{\rm X}$–T" relation and check its evolution with redshift.

All uncertainties in this work are at the 1σ confidence level, unless otherwise noted. We use a ΛCDM cosmology with $H_0 = 70$ km s^{-1} Mpc^{-1} and $\Omega_{\rm m} = 1 - \Omega_\Lambda = 0.3$.

⋆ Appendix A is only available in electronic form at http://www.aanda.org

Table 1. Cluster sample parameters and details of Chandra observations.

Cluster name	z	RA	Dec	Obs. ID	ACIS	Mode	Exp.	$N_{\rm H}$
		hh mm ss	° ′ ″				ks	10^{20} cm^{-2}
(1)	(2)	(3)	(4)	(5)	(6)	(7)	(8)	(9)
Abell 2125	0.246	15 41 12	+66 16 01	2207	I	VF	79.7	2.77
ZW CL 1454.8+2233	0.258	14 57 15	+22 20 33	4192	I	VF	91.4	3.22
MS 1008.1−1224	0.302	10 10 32	−12 39 23	926	I	VF	44.2	6.74
ZW CL 0024.0+1652	0.394	00 26 35	+17 09 39	929	S	VF	36.7	4.19
MS 1621.5+2640	0.426	16 23 36	+26 34 21	546	I	F	30.0	3.59
RX J1701.3+6414	0.453	17 01 24	+64 14 10	547	I	VF	49.5	2.59
CL 1641+4001	0.464	16 41 53	+40 01 46	3575	I	VF	44.0	1.02
V 1524.6+0957	0.516	15 24 40	+09 57 48	1664	I	VF	49.9	2.92
MS 0451.6−0305	0.539	04 54 12	−03 00 53	902	S	F	41.5	5.18
V 1121+2327	0.562	11 20 57	+23 26 27	1660	I	VF	66.9	1.30
MS 2053.7−0449	0.583	20 56 21	−04 37 51	1667	I	VF	43.5	4.96
V 1221+4918	0.700	12 21 26	+49 18 30	1662	I	VF	79.4	1.44
MS 1137.5+6625	0.782	11 40 22	+66 08 18	536	I	VF	117.5	1.18
RDCSJ 1317+2911	0.805	13 17 21	+29 11 19	2228	I	VF	111.3	1.04
RDCSJ 1350+6007	0.805	13 50 48	+60 06 54	2229	I	VF	58.3	1.76
RX J1716.4+6708	0.813	17 16 49	+67 08 26	548	I	F	51.5	3.71
MS 1054.4−0321	0.830	10 56 59	−03 37 37	512	S	F	67.5	3.67
WARPJ 1415.1+3612	1.013	14 15 11	+36 12 00	4163	I	VF	89.2	1.10

Column 1: cluster name. Column 2: Spectroscopic redshift tabulated in the literature. Columns 3, 4: right ascension and declination (Equatorial J2000, HH MM SS.S, +DD MM SS.S) of the centroid of the *Chandra* photon distribution in the 0.5–5 keV energy band assumed as the cluster center. Column 5: identification number of the observation. Column 6: detector where the aimpoint lies (I, for *ACIS-I* or S, for *ACIS-S*). Column 7: observation mode (F for FAINT or VF for VFAINT). Column 8: exposure time in ks corresponding to the nominal exposure filtered to exclude time periods of high background. Column 9: column density of Galactic hydrogen in units of 10^{20} cm^{-2}, obtained from the *Chandra* X-ray Center (CXC) Proposal Planning Tool Colden (Galactic Neutral Hydrogen Density Calculator): NRAO-compilation by Dickey & Lockman (1990).

2. *Chandra* data reduction and cluster analysis

We extracted from the *Chandra* archive the X-ray data of 18 galaxy clusters with redshift in the range $0.25 < z < 1.01$ and exposure time greater than 30 ks. Data reduction was performed using version 3.2.1 of the CIAO software (*Chandra* Interactive Analysis of Observations; see web page `http://cxc.harvard.edu/ciao/index.html`) and version 3.0.3 of the CALDB (Calibration Database). The sample is the same used by BR07 where the selection criteria and the data reduction are described in more detail. For clarification purposes we report here Table 1 of BR07 that lists the sample parameters and the details of the *Chandra* observations. Clusters are arranged in increasing redshift order.

The clusters of galaxies analyzed here appear as extended sources in the *Chandra* images. Differently from lower resolution instruments, *Chandra* is able to reveal point sources overimposed but not necessarily associated with the pointed cluster. Although such objects may be scientifically interesting in their own right (see discussion in BR07) investigators can now filter out any point source before fitting spectral models to the extended emission. For a correct analysis of the cluster properties the point source (non-thermal) emission should be subtracted from the cluster extended emission. Since one of the goals of our analysis is to estimate the impact of these point sources on the cluster properties, two approaches have been adopted:

- Point sources are identified using the CIAO Detect package WAVDETECT, which has the ability to work in complex fields with both point and extended sources (see BR07 for details on the procedure followed). The point sources are later removed from the event file using the *dmcopy* command.
- Point sources are *not* removed from the event file in an attempt to evaluate their effects on cluster parameters.

2.1. Background subtraction

The issue of background subtraction was carefully considered. For both spatial and spectral analyses, it is necessary to associate a background to the source events. For most of the clusters the background was measured locally, within the same target field, in a region free of point sources and in the vicinity of the cluster but not contaminated by the cluster emission. We checked that variations of the background intensity across the chip do not affect the background subtraction by comparing the count rates in the cluster and in the background regions at energies larger than 8 keV, where the signal from the cluster should be nil.

We also used the "blank-sky" data sets, following the steps and recommendations of the Markevitch's COOKBOOK[1]. The "blank-sky" background files were first reprocessed and reprojected to match the corresponding cluster observation gain and position. The background files were then normalized to the shorter exposure time of the cluster observations. The background events were extracted from the same region of the chip as the cluster to model spatial variations in the background. Obtaining background spectra from blank-sky data sets has the advantage to use the same region as the source, thus eliminating potential systematic errors caused by spatial variations of both the energy response and the effective area across the chip. The method remains, however, vulnerable to temporal variations in the spectrum of the particle background and also cannot easily account for the strong directional variation of the Galactic soft X-ray emission.

We performed consistency checks for several clusters of the sample. The properties obtained using background files derived from different regions of the target field and from the

[1] See `http://cxc.harvard.edu/contrib/maxim/acisbg/data/README` and `http://cxc.harvard.edu/contrib/maxim/acisbg/COOKBOOK`

"blank-sky" data sets are generally independent of the background used. For the two most nearby clusters of the sample, ZW CL 1454.8+2233 and Abell 2125, which cover a very extended region, we considered more appropriate to extract the background spectrum file from the "blank-sky" data-sets. For all the other clusters the background spectrum file was extracted from regions within the same target field.

2.2. Spatial analysis

2.2.1. Cluster surface brightness

The spatial analysis of the cluster X-ray emission was performed within images (with point sources excluded) in the energy range 0.5−5.0 keV. Under the assumption that the cluster gas is a symmetric isothermal sphere with a density profile described by a β-model (Cavaliere & Fusco-Femiano 1976):

$$n_{\rm gas}(r) = n_{0,\rm gas}\left(1+\left(\frac{R}{R_{\rm c}}\right)^2\right)^{-3\beta/2}, \quad (1)$$

the radial surface brightness was modelled accordingly as:

$$S(r) = S_0\left(1+\left(\frac{R}{R_{\rm c}}\right)^2\right)^{-3\beta+1/2} \quad (2)$$

where $R_{\rm c}$ is the core radius and β describes the slope of the density profile at large radii.

For each cluster the β-model fit to the surface brightness was performed using the exposure-corrected image with a constant background included in the fit. The best-fit parameters for $R_{\rm c}$ and β are listed in Table 2.

Even if the simple β-model is known to poorly describe the radial profile of *Chandra* highly resolved clusters (see Ettori et al. 2004), this model provides a good description of the cluster for our pourpose, that is to extrapolate luminosities to larger radii (see Sect. 3 and Paper II of Branchesi et al. 2007b). Exceptions are MS 1054.4−0321 and ZW CL 1454.8+2233. The former cluster presents a clear western substructure. The fit to the whole cluster provides unreasonably large values for β and $R_{\rm c}$ (as previously noted by Jeltema et al. 2001). The fit improves once we mask the western substructure from the main body of the cluster. The values of $R_{\rm c}$ and β in Table 2 for MS 1054.4−0321 were obtained in this way. For ZW CL 1454.8+2233 a single β-model is not an acceptable representation of the radial profile (see Notes on individual clusters in Sect. 4). Therefore no values of $R_{\rm c}$ and β are indicated in Table 2.

2.2.2. Definition of cluster extent

The spectrum of each cluster was extracted from a circular region centered on the X-ray centroid, out to a maximum radius which is hereafter referred to as spectral radius, $R_{\rm spec}$. This radius was chosen individually cluster by cluster so as to optimize the signal-to-noise ratio in order to determine the X-ray temperature of the cluster with maximum count statistics. To define this circular region around the centroid of the photon distribution we followed the procedure suggested by Tozzi et al. (2003).

A second extraction radius was adopted in order to consider the cluster extent where diffuse emission is still detectable. This radius, named $R_{\rm ext}$, is the radius where the cluster radial surface brightness merges into the background, and beyond which no further significant cluster emission is detected. Both $R_{\rm spec}$ and $R_{\rm ext}$ are listed in Table 2. The fraction of the net counts included in the $R_{\rm spec}$ extraction region is always between 0.80 and 0.95 of the net counts included in the $R_{\rm ext}$ extraction region once point sources have been excised from the cluster emission.

For each cluster, the events included in the extraction region were used to produce a spectrum file. This procedure was repeated considering the two above defined radii ($R_{\rm spec}$ and $R_{\rm ext}$) and approaches, that is filtering out or not the events associated to the point sources from the event file. We ended up with four spectrum files per cluster.

2.3. Spectral analysis

Spectra were extracted from within both the defined detection radii, $R_{\rm spec}$ and $R_{\rm ext}$, considering the two situations described above: cluster emission alone (from now on "cluster") and cluster plus point source emission (from now on "cluster+ps"). The Auxiliary Response File (ARF) and the Redistribution Matrix File (RMF) were computed from the same region where the spectra are extracted and were weighted by the detected counts in the restricted energy range (0.5–2.0 keV) where both the response and the thermal model do not vary much. When possible the weighted RMFs have been created using the new CIAO tool *mkacisrmf*[2], otherwise the previous tool *mkrmf* was used. For each cluster spectrum file (with or without point sources) the respective ARFs and RMFs were generated in order to account for the presence or absence of point sources. For each cluster spectrum file there are then three associated files, namely the background spectrum file and the two response matrices.

The spectra are then analyzed with the *XSPEC* package and fitted over the energy range 0.8–7.0 keV. The photons with energy below 0.8 keV were excluded to avoid systematic biases in the temperature determination due to uncertainties in the *ACIS* calibration at low energies. Ignoring energies above 7 keV has little effect on *Chandra* data due to the low effective area above that energy and the rapid S/N decrease of the thermal spectra. The spectra were fitted with an absorbed single-temperature thermal model called *wabs(mekal)* (Kaastra 1992; Liedahl et al. 1995). The absorbing hydrogen column was frozen at the Galactic value (as determined from radio HI maps, Dickey & Lockman 1990) in correspondence of the X-ray peak. The gas temperature, T, and the normalization, K, of the thermal component are the only free parameters. The best-fit temperatures were determined freezing the redshift at the values measured by spectroscopic observations (available in the literature) and fixing the metallicity (Z) at 0.3 $Z_\odot$. In the spectral fitting, we take into account the increased effective area at energies larger than 2 keV (due to a thin hydrocarbon layer, see Marshall et al. 2003) including in the fitting model the "positive absorption edge" (XSPEC model edge) described by Eq. (1) in Vikhlinin et al. (2005).

The spectral fit has been performed using both the Cash statistics (Cash 1979) and the χ^2 statistics (adopting a standard binning with a minimum of 20 photons per energy channel in the source plus background spectrum). The Cash statistics seems to be preferable for low-S/N spectra (Nousek & Shue 1989) when the number of counts available per bin is low. However the agreement between the models obtained with the two statistics (see Appendix A.1) makes us confident that both statistics

[2] *mkacisrmf* has been calibrated for the *ACIS-I* array plus *ACIS-S1,S2*, and *S3*. The tools creates response files intended for use with –120 °C data that has the time-dependent gain adjustment and CTI correction (if available) applied. There is no CTI correction for the back-illuminated *ACIS* chips, *S1* and *S3*.

Table 2. X-ray cluster parameters.

Cluster	R_c (kpc)	β	R_{spec} ($''$) (kpc)	R_{ext} ($''$) (kpc)	$N_{sources}$ (R_{spec}) (R_{ext})	$T_{R_{spec}}$ (keV)	$T_{R_{ext}}$ (keV)	$S_{0.5-2.0}$ (10^{-13} cgs)	$S_{2.0-10.0}$ (10^{-13} cgs)	L_{bol} (10^{44} cgs)
(1)	(2)	(3)	(4)	(5)	(6)	(7)	(8)	(9)	(10)	(11)
Abell 2125	182±12	0.54±0.02	153 591	241 931	13 26					
cl						$3.4^{+0.2}_{-0.2}$	$3.5^{+0.2}_{-0.2}$	$4.06^{+0.14}_{-0.14}$	$4.13^{+0.21}_{-0.22}$	$2.20^{+0.06}_{-0.07}$
cl+ps						$3.5^{+0.1}_{-0.1}$	$3.7^{+0.3}_{-0.2}$	$4.79^{+0.14}_{-0.14}$	$5.11^{+0.18}_{-0.23}$	$2.64^{+0.07}_{-0.07}$
ZW CL 1454.8+2233			128 512	200 800	4 7					
cl						$4.4^{+0.1}_{-0.1}$	$4.5^{+0.1}_{-0.1}$	$32.05^{+0.18}_{-0.18}$	$39.71^{+0.44}_{-0.47}$	$20.83^{+0.10}_{-0.10}$
cl+ps						$4.4^{+0.1}_{-0.1}$	$4.5^{+0.1}_{-0.1}$	$32.34^{+0.17}_{-0.18}$	$40.08^{+0.42}_{-0.41}$	$21.02^{+0.10}_{-0.11}$
MS 1008.1−1224	165±9	0.64±0.02	128 572	172 771	6 10					
cl						$6.0^{+0.4}_{-0.3}$	$6.1^{+0.4}_{-0.4}$	$8.76^{+0.19}_{-0.21}$	$15.67^{+0.60}_{-0.82}$	$10.28^{+0.29}_{-0.34}$
cl+ps						$6.2^{+0.4}_{-0.4}$	$6.3^{+0.4}_{-0.4}$	$8.97^{+0.20}_{-0.21}$	$16.32^{+0.63}_{-0.71}$	$10.65^{+0.30}_{-0.33}$
ZW CL 0024.0+1652*	128±10	0.67±0.03	69 367	118 628	2 7					
cl						$4.4^{+0.5}_{-0.4}$	$4.4^{+0.7}_{-0.5}$	$2.25^{+0.14}_{-0.14}$	$2.67^{+0.25}_{-0.28}$	$3.90^{+0.22}_{-0.22}$
cl+ps						$4.8^{+0.6}_{-0.6}$	$5.0^{+0.7}_{-0.7}$	$2.50^{+0.12}_{-0.15}$	$3.35^{+0.33}_{-0.40}$	$4.55^{+0.26}_{-0.29}$
MS 1621.5+2640	227±17	0.65±0.03	118 659	148 823	3 5					
cl						$7.5^{+1.1}_{-0.7}$	$7.5^{+1.3}_{-0.8}$	$4.31^{+0.21}_{-0.23}$	$7.78^{+0.41}_{-0.59}$	$11.07^{+0.54}_{-0.56}$
cl+ps						$7.8^{+1.1}_{-0.8}$	$8.0^{+1.1}_{-1.0}$	$4.79^{+0.18}_{-0.20}$	$8.99^{+0.66}_{-0.77}$	$12.69^{+0.79}_{-0.82}$
RX J1701.3+6414*	15±2	0.41±0.01	79 455	108 626	2 3					
cl						$4.5^{+0.4}_{-0.3}$	$5.0^{+0.6}_{-0.5}$	$2.61^{+0.14}_{-0.13}$	$3.26^{+0.24}_{-0.31}$	$6.27^{+0.28}_{-0.33}$
cl+ps						$4.8^{+0.5}_{-0.4}$	$5.5^{+0.6}_{-0.6}$	$2.62^{+0.15}_{-0.15}$	$3.55^{+0.26}_{-0.30}$	$6.54^{+0.28}_{-0.37}$
CL 1641+4001	151±18	0.77±0.06	54 317	89 519	3 6					
cl						$5.1^{+0.8}_{-0.7}$	$5.5^{+1.1}_{-0.9}$	$1.05^{+0.10}_{-0.11}$	$1.36^{+0.14}_{-0.19}$	$2.65^{+0.22}_{-0.22}$
cl+ps						$4.9^{+0.6}_{-0.6}$	$5.7^{+0.9}_{-0.7}$	$1.57^{+0.12}_{-0.13}$	$2.09^{+0.15}_{-0.19}$	$4.02^{+0.22}_{-0.26}$
V 1524.6+0957	302±27	0.80±0.05	79 488	148 916	3 10					
cl						$5.0^{+0.6}_{-0.5}$	$5.6^{+1.1}_{-0.8}$	$2.00^{+0.18}_{-0.20}$	$2.72^{+0.22}_{-0.33}$	$6.85^{+0.44}_{-0.52}$
cl+ps						$5.2^{+0.6}_{-0.6}$	$6.4^{+1.1}_{-0.9}$	$2.39^{+0.16}_{-0.17}$	$3.57^{+0.32}_{-0.44}$	$8.58^{+0.50}_{-0.64}$
MS 0451.6−0305	270±8	0.90±0.02	89 562	148 937	3 6					
cl						$9.4^{+0.7}_{-0.5}$	$9.6^{+1.0}_{-0.7}$	$9.81^{+0.20}_{-0.20}$	$20.84^{+1.12}_{-1.41}$	$50.43^{+2.56}_{-2.67}$
cl+ps						$9.3^{+0.6}_{-0.5}$	$9.8^{+1.0}_{-0.8}$	$9.96^{+0.19}_{-0.24}$	$21.41^{+0.99}_{-1.44}$	$51.77^{+2.44}_{-2.44}$
V 1121+2327	437±58	1.19±0.18	67 434	128 829	4 8					
cl						$4.5^{+0.5}_{-0.4}$	$5.5^{+1.1}_{-0.9}$	$1.38^{+0.11}_{-0.13}$	$1.72^{+0.19}_{-0.23}$	$5.44^{+0.37}_{-0.43}$
cl+ps						$4.5^{+0.5}_{-0.4}$	$5.9^{+1.2}_{-0.8}$	$1.58^{+0.13}_{-0.14}$	$2.08^{+0.15}_{-0.26}$	$6.38^{+0.35}_{-0.46}$
MS 2053.7−0449*	115±12	0.64±0.03	57 373	118 779	1 3					
cl						$4.3^{+0.5}_{-0.4}$	$5.1^{+1.4}_{-1.0}$	$1.26^{+0.12}_{-0.15}$	$1.51^{+0.19}_{-0.33}$	$5.69^{+0.46}_{-0.61}$
cl+ps						$4.5^{+0.6}_{-0.4}$	$5.2^{+1.4}_{-1.0}$	$1.28^{+0.13}_{-0.14}$	$1.56^{+0.20}_{-0.36}$	$5.81^{+0.43}_{-0.60}$
V 1221+4918	272±20	0.76±0.04	79 562	143 1020	3 8					
cl						$7.0^{+0.8}_{-0.7}$	$6.4^{+0.9}_{-1.0}$	$1.90^{+0.10}_{-0.11}$	$2.49^{+0.25}_{-0.27}$	$13.12^{+0.73}_{-0.75}$
cl+ps						$7.2^{+0.8}_{-0.3}$	$7.2^{+1.1}_{-0.8}$	$2.19^{+0.11}_{-0.12}$	$3.16^{+0.20}_{-0.26}$	$15.87^{+0.69}_{-0.78}$
MS 1137.5+6625	116±6	0.71±0.02	59 440	103 770	1 6					
cl						$6.2^{+0.6}_{-0.4}$	$5.7^{+0.6}_{-0.5}$	$1.61^{+0.09}_{-0.08}$	$1.82^{+0.10}_{-0.12}$	$13.62^{+0.48}_{-0.54}$
cl+ps						$6.3^{+0.6}_{-0.5}$	$6.0^{+0.6}_{-0.4}$	$1.99^{+0.07}_{-0.08}$	$2.37^{+0.15}_{-0.18}$	$17.17^{+0.58}_{-0.74}$
RDCSJ 1317+2911*	61±16	0.52±0.04	30 222	69 518	1 5					
cl						$3.7^{+1.2}_{-0.8}$	$2.4^{+0.9}_{-0.6}$	$0.17^{+0.04}_{-0.05}$	$0.06^{+0.02}_{-0.03}$	$1.28^{+0.36}_{-0.37}$
cl+ps						$5.8^{+2.9}_{-1.6}$	$4.1^{+1.8}_{-1.3}$	$0.20^{+0.04}_{-0.04}$	$0.15^{+0.02}_{-0.06}$	$1.62^{+0.23}_{-0.31}$
RDCSJ 1350+6007	261±43	0.70±0.07	64 481	128 962	3 9					
cl						$4.1^{+0.8}_{-0.6}$	$3.7^{+1.2}_{-0.7}$	$0.77^{+0.12}_{-0.13}$	$0.51^{+0.06}_{-0.12}$	$6.19^{+0.76}_{-0.88}$
cl+ps						$4.6^{+0.9}_{-0.7}$	$4.6^{+1.3}_{-0.8}$	$0.96^{+0.12}_{-0.14}$	$0.84^{+0.09}_{-0.15}$	$8.14^{+0.73}_{-0.93}$
RX J1716.4+6708	119±11	0.66±0.03	59 446	108 817	3 9					
cl						$6.5^{+0.9}_{-0.8}$	$6.0^{+1.1}_{-0.7}$	$1.31^{+0.09}_{-0.11}$	$1.62^{+0.22}_{-0.27}$	$13.15^{+0.93}_{-1.16}$
cl+ps						$7.8^{+1.2}_{-0.9}$	$8.1^{+1.7}_{-1.2}$	$1.47^{+0.10}_{-0.11}$	$2.35^{+0.25}_{-0.36}$	$16.76^{+1.22}_{-1.52}$
MS 1054.4−0321	520±32	1.38±0.11	84 636	128 972	2 6					
cl						$8.3^{+0.7}_{-0.7}$	$7.8^{+1.0}_{-0.9}$	$2.96^{+0.10}_{-0.12}$	$4.59^{+0.37}_{-0.37}$	$34.83^{+1.66}_{-1.82}$
cl+ps						$8.9^{+0.7}_{-0.7}$	$8.6^{+0.9}_{-0.9}$	$3.13^{+0.10}_{-0.10}$	$5.17^{+0.34}_{-0.38}$	$38.26^{+1.56}_{-1.75}$
WARPJ 1415.1+3612	68±7	0.60±0.02	39 316	79 632	2 4					
cl						$6.2^{+0.8}_{-0.7}$	$6.3^{+1.0}_{-0.9}$	$0.67^{+0.05}_{-0.06}$	$0.75^{+0.07}_{-0.12}$	$11.88^{+0.71}_{-0.91}$
cl+ps						$7.0^{+0.9}_{-0.8}$	$7.1^{+1.3}_{-1.0}$	$0.79^{+0.06}_{-0.07}$	$0.97^{+0.06}_{-0.11}$	$13.10^{+0.83}_{-0.96}$

are a good choice. Throughout this paper we will use the χ^2 statistics for the only reason that, unlike the Cash statistics, the χ^2 statistics gives a measure of the absolute goodness of the fit. We verified that all our spectra are well–fitted by single–temperature models: the best-fit models have a reduced $\chi^2 \sim 1$ and a null-hypothesis probability above 15% (except for ZW CL 1454.8+2233, see Notes on individual clusters in Sect. 4).

Once the models with the best-fit parameters were determined *XSPEC* has been used to calculate the cluster flux over different energy bands and the cluster bolometric luminosity. The errors on the cluster parameters are obtained in *XSPEC* from

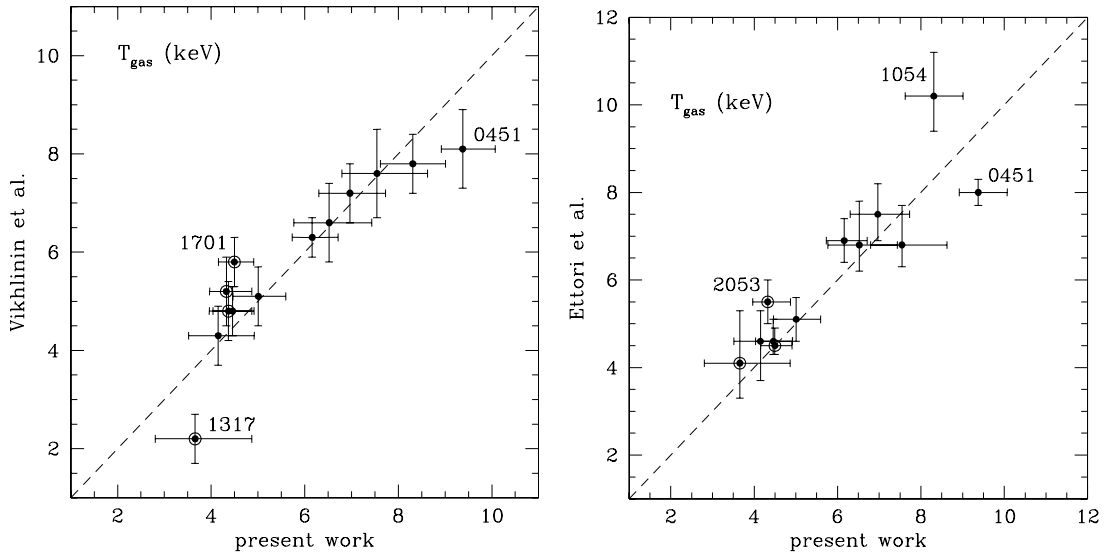

Fig. 1. Comparison between the estimates of the gas temperature by VI02 (*left panel*) and our estimate for the 13 clusters in common. To the *right panel* the same comparison is shown for the 12 clusters in common with ET04. The circled points indicate clusters assumed by VI02 to be cooling core clusters. Like us, ET04 did not excise any excess surface brightness central region due to the presence of "cooling flows". In both panels the dashed line is equality between the two works.

the distribution of the values around the best-fit value of the spectral analysis. The quoted luminosities were corrected for the effect of absorption by the Galactic HI column density at low energies. Hereafter the unabsorbed bolometric luminosity is called bolometric luminosity or $L_{\rm bol}$.

Since the quality of the fits is better inside the region that maximizes the signal to noise ratio, the temperatures estimated within $R_{\rm spec}$, i.e. $T_{R_{\rm spec}}$, are considered more representative of the actual average temperature of the gas. However the two temperatures are consistent within the errors with no significant systematic differences between them. For the luminosities we used instead the $R_{\rm ext}$ radius in order to take into account the faint brightness tails at the cluster periphery as well as the point sources in those regions. The choice of the different radii ($R_{\rm spec}$ for the determination of temperature and $R_{\rm ext}$ for the determination of luminosity) is justified in Appendix A.2 where a more detailed description of the analysis of the best-fit cluster parameters is given.

The cluster parameters are listed in Table 2. The columns contain the following information:

- Column 1: the first line gives the cluster name, the second and third lines indicate how parameters are derived, if for the cluster alone or for the cluster plus point sources. An asterisk close to the cluster name indicates that the cluster has been classified as a possible cooling core by Vikhlinin et al. (2002)
- Columns 2, 3: core radius in kpc and β.
- Column 4: radius (spec) which maximizes the S/N, in arcsec and kpc.
- Column 5: radius (ext) where the cluster X-ray radial profile becomes flat, in arcsec and kpc.
- Column 6: number of point sources detected (and removed) within $R_{\rm spec}$ and $R_{\rm ext}$, respectively. These point sources were detected either in the soft or in the hard energy band (see BR07 for details). The column lists also faint sources which become significant ($S/N > 3$) in the full energy band (0.5−7.0 keV).
- Column 7: temperature estimated within $R_{\rm spec}$ in keV.
- Column 8: temperature estimated within $R_{\rm ext}$ in keV.
- Columns 9, 10: observed soft and hard flux estimated within $R_{\rm ext}$ in units of 10^{-13} erg cm^{-2} s^{-1}.
- Column 11: unabsorbed X-ray bolometric luminosity estimated within $R_{\rm ext}$ in units of 10^{44} erg s^{-1}.

3. Comparison with other authors

Two recent works, one by Vikhlinin et al. (2002) (from now on VI02) and one by Ettori et al. (2004) (from now on ET04), have 13 and 12 clusters respectively in common with us. It is thus very instructive to compare our estimates of the gas temperatures and bolometric luminosities with their results in order to check for the presence of any systematic bias due to the different approaches adopted. Of particular importance is the radius used to measure the properties of the clusters.

3.1. Temperatures

A comparison of our temperatures with those of VI02 is shown in Fig. 1 (panel to the left). Differently from us, VI02 excluded the central 100 h_{50}^{-1} kpc region in the cooling core clusters. The agreement is very good: a mean ratio of 1.02 ± 0.04 between VI02 temperatures and ours has been found. In three out of four clusters assumed by VI02 to be possible cooling core (indicated by an asterisk in Table 2) they report higher temperatures. The largest difference, significant at 2.9σ, is found for RX J1701+6414. For the fourth cluster, RDCSJ 1317+2911, we find instead a higher temperature, $kT = 3.7^{+1.2}_{-0.8}$ keV against the value found by VI02 of $kT = 2.2^{+0.5}_{-0.5}$ keV. The difference is significant at the 2.2σ level. For MS 0451.6−0305 the temperature difference, significant at 2σ confidence level, can be explained in terms of the new calibrations that we have applied.

The comparison with ET04 (their values vs. ours) shows that their temperatures are on average a factor of 1.06±0.03 higher than ours (see panel to the right in Fig. 1). The largest absolute values of the differences (significant at $>2\sigma$) are found for MS 0451.6−0305 (3.6σ), MS 1054−0321 (2.5σ) and MS 2053.7−0449 (2.2σ). All these discrepancies are discussed in the notes on individual clusters (Sect. 4).

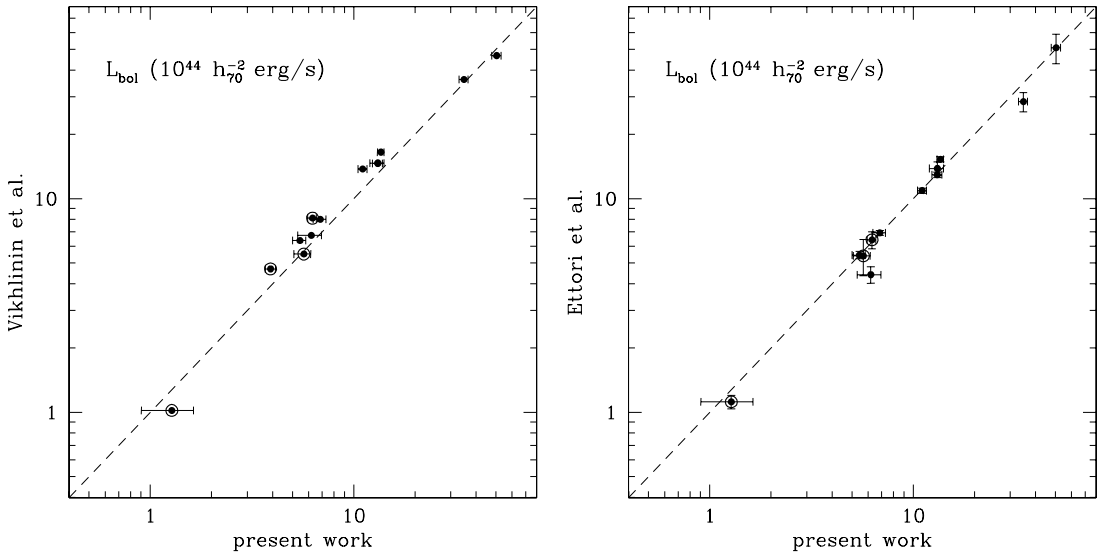

Fig. 2. Comparison between the luminosities estimated by VI02 and by us for the 13 clusters in common (*left panel*) and by ET04 and by us for the 12 clusters in common (*right panel*). The circled points indicate the clusters assumed by VI02 to be cooling core clusters. In both panels the dashed line is equality between the two works.

3.2. Luminosities

It has to be noted that both VI02 and ET04 derived cluster luminosities within areas often quite different from the areas we used. Many authors discuss the importance of the choice of the radius within which cluster properties are measured, especially when comparing integrated cluster properties with theoretical predictions or simulations. A common choice is to use as radius a fixed linear size, which has the obvious benefits in terms of simplicity. VI02 used a fixed radius of 2 h_{50}^{-1} Mpc, corresponding to 1.4 h_{70}^{-1} Mpc in our cosmology. Since VI02 excluded the central 100 h_{50}^{-1} kpc regions in the cooling core clusters, they accounted for the missed flux by multiplying by a factor 1.06 typical of a β-model cluster.

Other authors define a "more physical" radius which requires the knowledge of the cluster mass profile so that the mean enclosed density is a fixed factor above the critical density of the Universe. This approach is followed by ET04 who define R_{500}, which corresponds to an overdensity $\Delta_z = 500 \times \Delta_v(z)/(18\pi^2)$ with respect to the critical density of the Universe at redshift z. Their luminosities were computed by extrapolating to R_{500} the values measured within $R_{\rm spec}$ by means of an isothermal β-profile. Like us, ET04 did not excise any excess surface brightness central region due to the presence of "cooling flows". Differently from these authors we used an "observed" radius which indicates the region where the emission is detected ($R_{\rm ext}$, see Sect. 2.2.2). The VI02 radii differ from our radii by a factor ranging from 1.04 up to 2.7. Also the ET04 radii are larger than our radii by a factor ranging from 1.03 up to 1.55, except for RDCSJ 1350+6007 that has a ET04 radius about 30% less than ours.

The comparison between the VI02 luminosities and ours gives a mean ratio of 1.10 ± 0.04 (see left panel of Fig. 2). The fact that the VI02 luminosities are on average 10% higher than our estimates may be explained by the larger regions (radius of 2 h_{50}^{-1} Mpc) used by them. The mean ratio between the ET04 luminosities and ours is 0.96 ± 0.03 (see right panel of Fig. 2).

To check if any systematic bias is introduced by our choice of the radius, we extrapolate our luminosities to the radii adopted by the other authors. The correction to be applied to our data

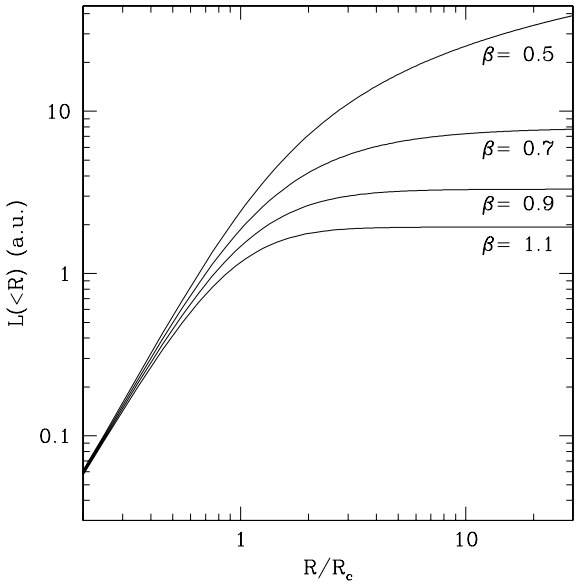

Fig. 3. The luminosity computed within a radius R as a function of the ratio between the radius R and the core radius $R_{\rm c}$ for different β values.

was obtained assuming that the gas density profile is described by the β-model (see Eq. (1)) defined by our estimates for the core radius, $R_{\rm c}$, and for β (see Sect. 2.2.1). It has to be noted that these corrections do not depend on the ratio between the different integration radii only but depend strongly on β and $R_{\rm c}$. This can be clearly seen in Fig. 3 which shows the luminosity computed within a given radius R as a function of $R/R_{\rm c}$, for different values of β.

The comparison between VI02 luminosities and our luminosities extrapolated to 1.4 h_{70}^{-1} Mpc gives a very good agreement (see left panel of Fig. 4). Excluding the most discrepant cluster in the plot, RDCSJ 1317+2911 (which has although very large errorbar values) the mean ratio between the VI02 luminosities and ours is of 0.99 ± 0.03. Note that the corrections to be applied to our luminosities for such an extrapolation are not negligible. They range from ∼0.9 to ∼1.25 with a median value of

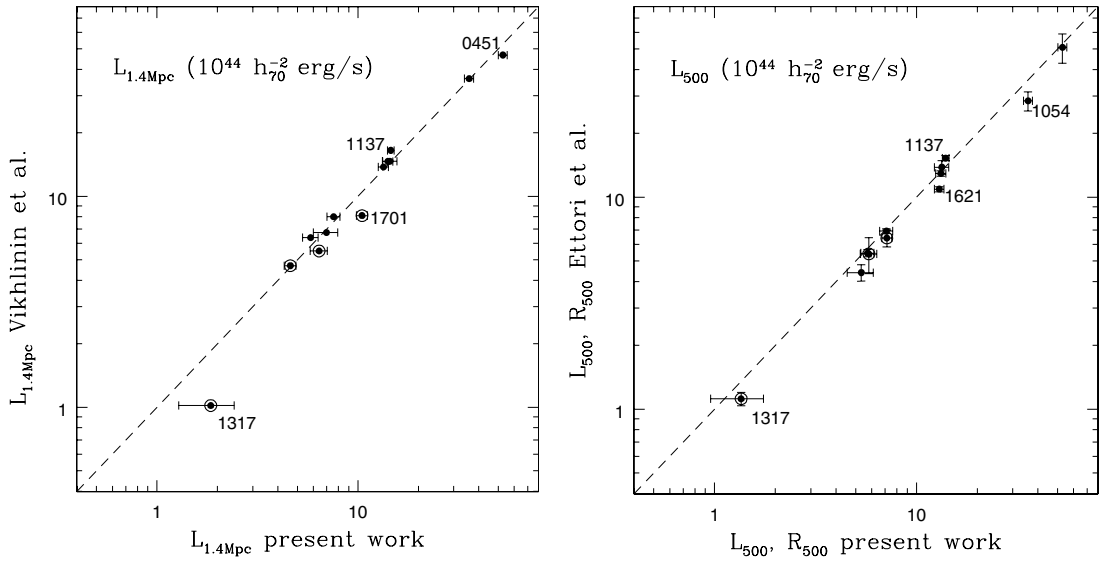

Fig. 4. (*Left panel*) Comparison between the luminosities estimated by VI02 and our luminosities extrapolated to 1.4 h_{70}^{-1} Mpc for the 13 clusters in common. The circled points indicate the clusters assumed by VI02 to be cooling core clusters. (*Right panel*) Comparison between the luminosities estimated by ET04 and our luminosities extrapolated to R_{500} for the clusters in common. In both panels the uncertainties on the extrapolated luminosities are combined errors which take into account both the errors obtained in the spectral analysis by XSPEC and the uncertainties on the β-model for the gas density profile. In both panels the dashed line is equality between the two works.

1.10 (mean 1.13). Similar results were obtained using the VI02 estimates of R_c and β, instead of ours, to extrapolate to the VI02 radius. The clusters with the largest absolute values ($>2\sigma$) of the difference between our and VI02 luminosities are indicated in the figure: the possible cooling core cluster RX J1701.3+6414 (4.0σ), MS 1137.5+6625 (3.2σ) and MS 0451.6-0305 (2.3σ).

In the comparison with ET04 (see right panel in Fig. 4) we extrapolated our luminosities to R_{500}. This radius was calculated assuming our estimates for the cluster temperature, for the core radius and β (see Paper II of Branchesi et al. 2007b for more details). If one compares the right panel of Fig. 4 with the right panel of Fig. 2, it can be noted that the extrapolation to R_{500} does not improve the comparison with ET04. In fact the mean ratio between the ET04 luminosities and ours changes from 0.96 ± 0.03 to 0.93 ± 0.02. A similar result is obtained if we extrapolate our luminosities using their estimates for R_{500}, R_c and β. In the right panel in Fig. 4 cluster luminosities which deviate more than $>2\sigma$ from the ET04 estimates are indicated with the cluster name. They are MS 1621.5+2640 (4.0σ), MS 1054.4-0321 (3.0σ), MS 1137.5+6625 (2.7σ).

In summary the comparison with VI02 suggests that the correction for the different radii is important if we want to be consistent with their luminosities. Their radius is in fact quite larger than ours, but after corrections are implemented the agreement is very good. The comparison with ET04 instead suggests that the correction for the different radii are smaller than the measurement uncertainties and hence could be neglected. The agreement between our and ET04 measurements is good, although there is a very weak systematic offset in the sense that ET04 luminosities tend to be lower than our estimates.

In Paper II of Branchesi et al. (2007b) we describe in detail why it is important to extrapolate all luminosities to an homogeneous radius (e.g., R_{500}) when the observed L_{bol}–T relations are compared with the self-similarity evolution predictions.

4. Notes on individual clusters

4.1. MS 0451.6−0305

MS 0451.6−0305 is the most luminous cluster in the EMSS sample (Gioia et al. 1990). We found a best-fit temperature within R_{spec} of $kT = 9.4^{+0.7}_{-0.5}$ keV, which disagrees with the estimates of $kT = 8.1^{+0.8}_{-0.8}$ keV and of $kT = 8.0^{+0.3}_{-0.3}$ keV found by VI02 and ET04, respectively (see Fig. 1).

In a more recent article Donahue et al. (2003) analyzed the same *Chandra* data. They discuss in detail the results of applying a soft-energy, time-dependent correction to the *ACIS-S*, which however they consider uncertain. Thus without applying the correction the authors find that MS 0451.6-0305 is consistent with an isothermal cluster with kT ranging from 10 keV to 10.6 keV ($\pm$1.6 keV at the 90% confidence level), and with intracluster Fe abundance range between 0.32 and 0.40 ($\pm$0.13 solar at the 90% confidence level). Including the correction in their analysis, they may explain the discrepancy between their best-fit temperature and the temperature obtained by VI02. However they find that to be acceptable the fit requires a second component that could be either a cooler thermal component or a steep power-law component.

Our data have been analyzed applying the time-dependent correction as suggested by the CXC (*Chandra* X-ray Center). Our correction is more accurate since the CALDB used by us is more recent than the one used by Donahue et al. (2003). The more recent calibration adopted can explain the temperature discrepancies with respect to VI02 and ET04 (see Fig. 1). Our estimate of $kT = 9.4^{+0.7}_{-0.5}$ keV is consistent with the *ASCA* measure of $kT = 10.2^{+1.5}_{-1.3}$ keV (Mushotzky & Scharf 1997). We detected six very faint sources ($S_{0.5-1\ 0keV} < 10^{-14}$ erg cm^{-2} s^{-1}) within the more extended aperture radius $R_{ext} = 100''$ (see BR07). The cluster temperature does not change much if one includes the point sources ($kT = 9.6^{+1.0}_{-0.7}$ keV vs. $kT = 9.8^{+1.0}_{-0.8}$ keV).

4.2. MS 1054.4−0321

MS 1054−0321 is the highest redshift ($z = 0.83$) cluster in the EMSS and shows a significant amount of substructure with the *Chandra* resolution (Jeltema et al. 2001). As mentioned in Sect. 3 the temperature and luminosity estimates obtained by ET04 disagree with ours (see right panels of Fig. 1 and Fig. 4, respectively). ET04 estimated both the temperature and the best-fit surface brightness profile from the main body of the cluster after masking with a 36″ radius circle the cooler region at RA, Dec (2000) = $10^{\rm h}56^{\rm m}55\overset{\rm s}{.}7, -03°37'37''$. Since we did not exclude this region a lower temperature and a higher luminosity are obviously estimated. In addition, this cluster is an example of how the X-ray temperatures based on *Chandra* data change as new calibrations become available. An analysis of XMM-Newton data by Gioia et al. (2004) results in a temperature $kT = 7.2^{+0.7}_{-0.6}$ keV, which is much lower than the temperature previously reported from *ASCA* data, $kT = 12.3^{+3.1}_{-2.2}$ keV (Donahue et al. 1998), and also somewhat lower than the first *Chandra* temperature, $kT = 10.4^{+1.7}_{-1.5}$ keV, determined by Jeltema et al. (2001). The temperature measurement of MS 1054−0321 by Jeltema et al. (2001) probably suffered from the absence of a low-energy correction, called ACISABS, which was not available at the time of their analysis. VI02 used the same *Chandra* observations and derived a lower value for the temperature, $kT = 7.8 \pm 0.6$ keV, in agreement with us and with the determination by Tozzi et al. (2003) of $kT = 8.0 \pm 0.5$ keV. All quoted uncertainties are at 90% confidence level except for the last one which is at 68%.

As described in Sect. 2.3 we obtain an estimate for the temperature of $kT = 8.3^{+0.7}_{-0.7}$ keV within $R_{\rm spec} = 80''$. We applied the new available procedure to correct for the quantum efficiency. As observed in Jee et al. (2005) this new procedure (certainly more accurate) tends to yield a higher temperature than the ACISABS prescription. Jee et al. (2005) find a temperature of kT = $8.9^{+1.0}_{-0.8}$ keV, within 90″. Using the more extended region ($R_{\rm ext}$= 130″) we estimate a temperature of $kT = 7.8^{+0.9}_{-1.0}$ keV.

4.3. MS 1137.5+6625

MS 1137.5+6625 is the second most distant cluster in the EMSS sample. Our best-fit temperature of $kT = 6.2^{+0.4}_{-0.5}$ keV is consistent with the estimates obtained by VI02 ($kT = 6.3^{+0.4}_{-0.4}$ keV) and by Borgani et al. (2001) ($kT = 5.7^{+0.8}_{-0.7}$ keV). The three temperatures above are computed within an aperture radius of about 60″. Our temperature is also consistent with the one determined from *ASCA* data, $kT = 5.7^{+0.8}_{-0.7}$ keV, by Donahue et al. (1999). Ettori et al. (2004) and Tozzi et al. (2001) found $kT = 6.9^{+0.5}_{-0.5}$ keV and $kT = 7.0^{+0.5}_{-0.5}$ keV, respectively, within a smaller region of about 50″ radius.

4.4. RDCSJ 1317+2911

Despite this cluster is classified by VI02 as a possible cooling core system, our temperature estimate ($kT = 3.7^{+1.2}_{-0.8}$ keV) is higher than the value found by VI02 ($kT = 2.2^{+0.5}_{-0.5}$ keV) even though we did not exclude the cooling flow region in our analysis. This discrepancy, visible in Fig. 1 (left panel), might be explained considering that RDCSJ 1317+2911 has a low signal to noise ratio. A discrepancy in the same direction has been found by ET04 ($kT = 4.1^{+1.2}_{-0.8}$ keV) and by Tozzi et al. (2003) ($kT = 4.0^{+1.3}_{-0.8}$ keV). Tozzi et al. (2003) argue that such a difference can be ascribed to differences in the procedure used to remove faint point sources within the extraction region, which becomes critical for clusters with low S/N such as this one. This cluster illustrates the relevance of point source subtraction when dealing with low number counts. In fact the point sources increase by about 60% the best-fit temperature of RDCSJ 1317+2911 as one can see in Fig. 5. The low S/N implies also large errors on the luminosity and justifies the disagreement between our results and ET04 shown in Fig. 4. The uncertainties on the luminosity are much larger than the difference expected in the luminosity when using different radii.

4.5. ZW CL 1454.8+2233

This cluster is very discrepant with respect to the behavior of other clusters in the $L_{\rm bol}$–T relationship given in Sect. 6. ZW CL 1454.8+2233 was identified as a relaxed cluster hosting a massive cooling flow by Allen et al. (1996) using *ASCA* and *ROSAT* data. A 10 Ks *Chandra* observation revealed the presence of two surface brightness edges on opposite sides of the X-ray peak which were discussed by Mazzotta et al. (2001) under the hypothesis of a merging scenario. The 90 Ks *Chandra* observation analyzed by us confirms a very disturbed morphology. The surface brightness profile is inadequately described by a β-model (the probability to accept the spatial fit is lower then 0.1%) both for the presence of the cooling core and for the presence of some surface brightness jumps. For this reason no values for $R_{\rm c}$ and β are indicated in Table 2. On the other hand for the spectral analysis a single-temperature model was accepted. The null-hypothesis probability is about 5%, a little less than the threshold indicated in Sect. 2.3. We tried also to use a cooling flow spectral model *mkcflow* added to a *mekal* model but the improvement in the fit is minimal. The thermal complexity of this cluster, which could explain the peculiarity of its behavior in the $L_{\rm bol}$–T relation, convinced us to exclude it from the fit of the $L_{\rm bol}$–T relation.

4.6. MS 1621.5+2640

The best-fit temperature that we obtained for MS 1621+2640 ($kT = 7.5^{+1.1}_{-0.7}$ keV) is 10% greater than the temperature obtained by ET04 ($kT = 6.8^{+0.9}_{-0.5}$ keV) but in better agreement with the estimate by VI02 ($kT = 7.6^{+0.9}_{-0.9}$ keV). Also our luminosity extrapolated to R_{500} disagree with the estimate of ET04 by an amount on order of 18%. This discrepancy could be partly accounted for by the fact that we found a temperature of the gas higher with respect to ET04 temperature.

4.7. CL 1641+4001

For this cluster the effect of point sources on the cluster thermal emission is particularly important. In the region covered by the cluster we found six sources, two of which with a total flux $\geq 50\times 10^{-14}$ erg cm^{-2} s^{-1}. When the point sources are included in the fit the luminosity increases of ∼50%. On the other hand these sources have a small (∼3%) impact on the cluster temperature.

4.8. MS 2053.7−0449

MS 2053.7−0449 is assumed to be a cooling core cluster by VI02. They measure a temperature of $kT = 5.2^{+0.7}_{-0.7}$ keV. Our best-fit temperature is $kT = 4.3^{+0.5}_{-0.4}$ keV within the $R_{\rm spec}$ region, and $kT = 5.1^{+1.4}_{-1.0}$ keV when the larger radius $R_{\rm ext}$ is used. Our lower temperature estimate could be explained by fact that the

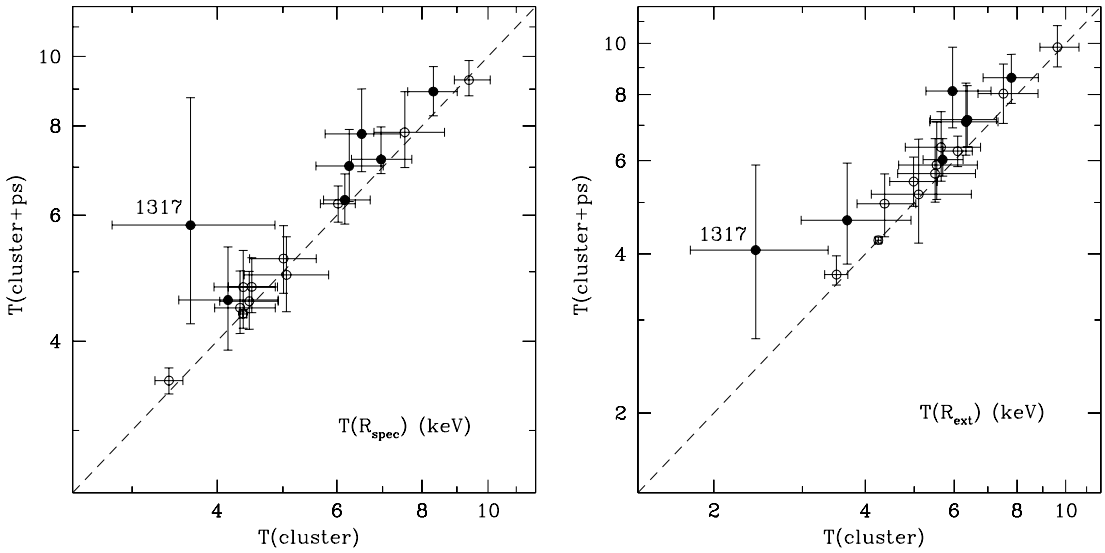

Fig. 5. Temperature of clusters plus point sources versus temperature of clusters without point sources. *Left panel* refers to $R_{\rm spec}$ and *right panel* to $R_{\rm ext}$. Solid circles indicate high-z ($z > 0.7$) clusters and open circles indicate low-z ($z < 0.7$) clusters. In both panels the dashed line is equality between the two temperatures.

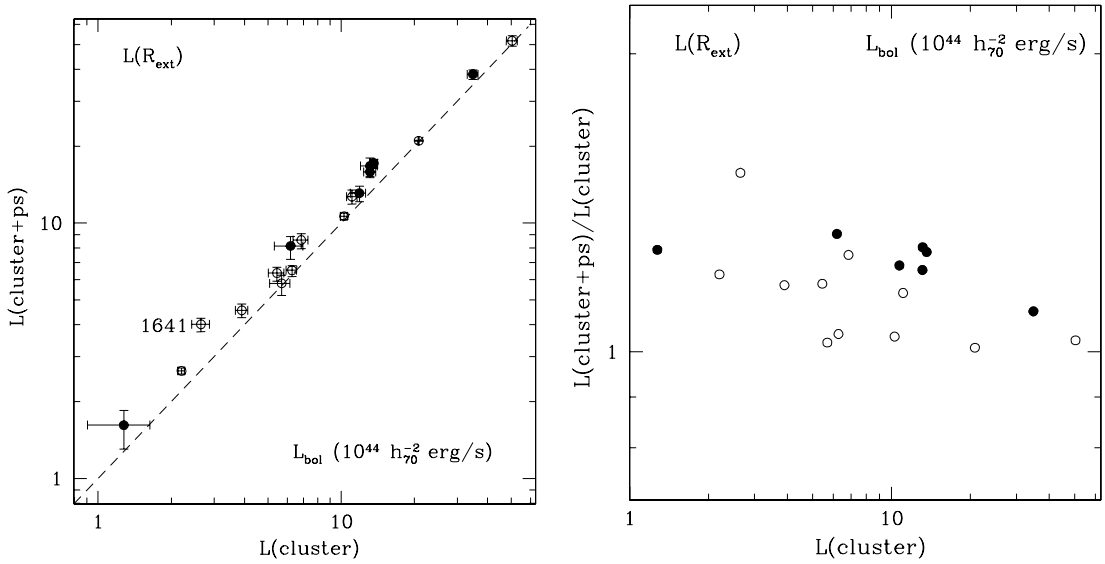

Fig. 6. *(Left panel)* Luminosity of clusters plus point sources versus luminosity of clusters without point sources. The dashed line is equality between the two luminosities. *(Right panel)* Ratio between luminosity of the clusters plus point sources and luminosity of the clusters without point sources versus luminosity of the clusters alone. Solid circles refer to high-z clusters and open circles refer low-z clusters.

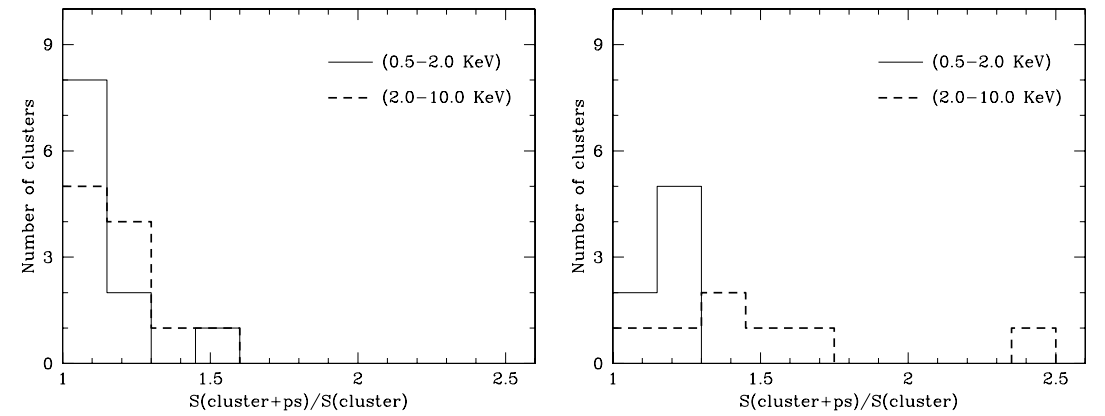

Fig. 7. Histograms of the ratio between the flux of the clusters plus point sources and the flux of clusters without point sources. The *left panel* is for clusters with redshift < 0.7 and the *right panel* for clusters with redshift> 0.7. The solid line indicates the soft energy band (0.5–2.0 keV) and the dashed line indicates the hard energy band (2.0–10.0 keV).

possible cooling region is not excluded in our analysis. ET04 did not exclude the cooling core and found a temperature of $kT = 5.5^{+0.5}_{-0.5}$ keV larger than VI02 and our temperature estimate. However, Maughan et al. (2007) found a value for the temperature of $kT = 4.1^{+0.5}_{-0.4}$ keV or $kT = 4.2^{+0.9}_{-0.6}$ keV according if the central region is taken into account or not. From the comparison with the results of the above mentioned authors it seems that the cluster may not be a cooling core.

5. Point source contribution to cluster thermal emission

The effect of the point sources on the best-fit temperature is shown in Fig. 5. The plots show the estimated temperature for clusters plus point sources ($T_{\rm cluster+ps}$) versus the temperature for clusters without point sources ($T_{\rm cluster}$). The left panel refers to temperatures estimated within $R_{\rm spec}$ while the right panel refers to $R_{\rm ext}$. Obviously the number of point sources within $R_{\rm ext}$ is higher than within $R_{\rm spec}$. The most discrepant point in Fig. 5 has been discussed in the note of RDCSJ 1317+2911 (Sect. 4).

The effect of the point sources on the temperature estimate is evident (especially within $R_{\rm ext}$). In addition a mild dependence on the redshift is also present. The average of the ratio $r_T = T_{\rm cluster+ps}/T_{\rm clusters}$ gives a temperature excess of (8 ± 3)% within $R_{\rm spec}$ and (13 ± 4)% within $R_{\rm ext}$. Splitting the sample at $z = 0.7$ we get, respectively, (16 ± 7)% and (24 ± 8)% for $z > 0.7$ and (3 ± 1)% and (6 ± 1)% for $z < 0.7$.

The left panel of Fig. 6 represents the same plot of Fig. 5 for cluster luminosities: $L_{\rm cluster+ps}$ is plotted versus $L_{\rm cluster}$. A different way of presenting these data is illustrated to the right of Fig. 6 where the ratio $r_L = L_{\rm cluster+ps}/L_{\rm cluster} \approx (1 + L_{\rm ps}/L_{\rm cluster})$ is plotted versus $L_{\rm cluster}$. This is a way to examine the "contrast" of point source luminosity with respect to cluster luminosity. The plot shows a mild trend for the luminosity "contrast" to decrease with increasing cluster luminosity. Similarly to the temperature, the contrast in luminosity due to the point sources is more pronounced in distant clusters. The low-z clusters (open circles in Fig. 6, right) are generally below the high-z clusters (solid circles) in the same luminosity range. The average of r_L gives an over-luminosity of (17 ± 3)% with (22 ± 3)% for high-z clusters and of (14 ± 4)% for low-z clusters. These values are similar, but more significant, than those for r_T computed within $R_{\rm ext}$.

Given the probably different X-ray spectrum of clusters and point sources (possibly AGN) we have investigated the contribution of the point sources to the flux in the soft and hard energy bands separately, by computing the two ratios $r_S = S_{\rm cluster+ps}/S_{\rm cluster}$ for both 0.5–2.0 keV and 2.0–10.0 keV energy bands. The histograms of such ratios are shown, overplotted, in Fig. 7, where the solid (dashed) line represents the soft (hard) band. Clusters with redshift < 0.7 are shown to the left and those with redshift > 0.7 to the right. The figure indicates that the point source contribution is higher in the hard band, as one might expect if the point sources have a spectrum harder than clusters. This effect is more evident for the distant clusters (right panel). It has to be noted that in both energy bands the excess in flux is mainly due to some bright objects (projected onto or belonging to the cluster) rather than to many faint sources.

The data suggest that there is a mild tendency for distant clusters ($z > 0.7$) to be more affected by point sources. If real, this effect would naively imply that the line of sight to farther clusters intercepts a higher number of bright point sources. However, this is contrary to what expected from the fact that distant clusters cover an average angular area which is ~50% that covered by nearby clusters, and that the flux is about half the flux of nearby clusters. If point sources are mostly unrelated to the clusters, these two effects would compensate and the point source contribution to the cluster overall budget should be independent of the cluster redshift. The observational result of seeing a larger number of point sources in distant clusters goes in the direction of having more sources belonging to high-z clusters. Indeed in a recent paper BR07 found an overdensity of point sources in clusters with respect to the field, and an indication in the hard band that the excess is mainly associated to high-z cluster.

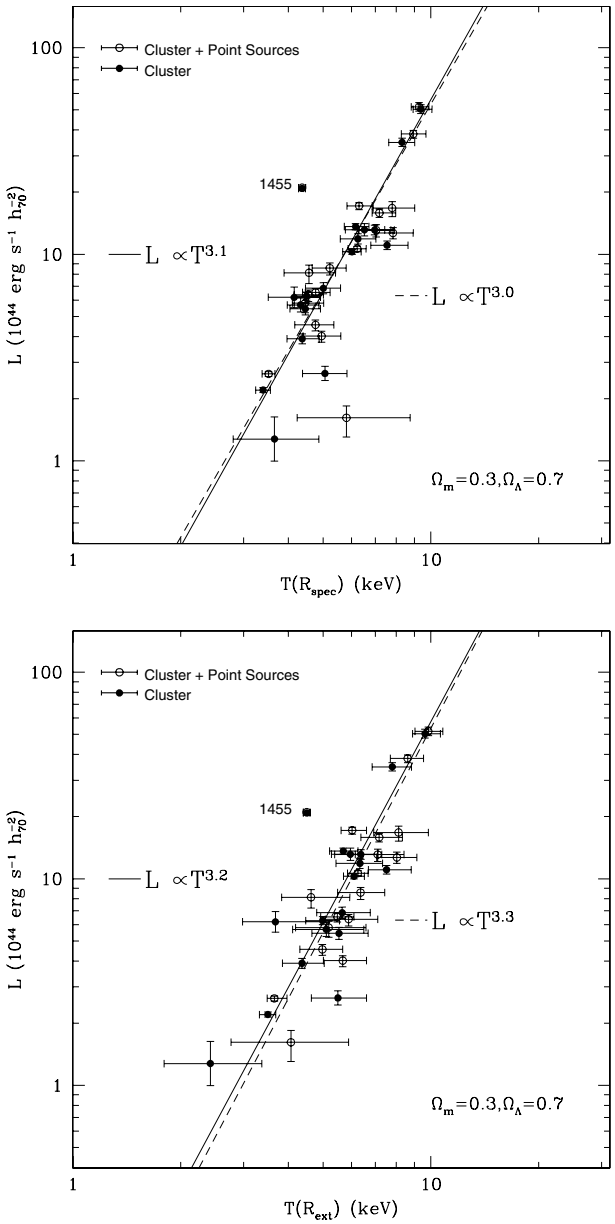

Fig. 8. Cluster bolometric luminosity versus temperature relationship. The open circles indicate cluster plus point source emission and the solid circles indicate cluster emission alone. The dashed and solid lines are the best-fit of the $L_{\rm bol}$–T relation to the open and solid circles data respectively. The solid circle indicated as 1455 represents the cluster ZW CL 1454.8+2233 which was removed from the fit (see Notes on individual clusters in Sect. 4).

Table 3. $L_{\rm bol} - T$ best-fit parameters.

$L_{\rm bol} - T(R_{\rm spec})$	Cluster	Cluster + Point Sources
α	$+3.09^{+0.35}_{-0.28}$	$+3.00^{+0.31}_{-0.26}$
$\log C$	$+1.06^{+0.04}_{-0.04}$	$+1.06^{+0.04}_{-0.04}$
$\chi^2_{\rm min}$/d.o.f.	14.77/15	17.54/15
$L_{\rm bol} - T(R_{\rm ext})$	Cluster	Cluster + Point Sources
α	$+3.23^{+0.51}_{-0.38}$	$+3.29^{+0.58}_{-0.43}$
$\log C$	$+1.04^{+0.07}_{-0.06}$	$+1.00^{+0.06}_{-0.06}$
$\chi^2_{\rm min}$/d.o.f.	12.24/15	14.25/15

6. The $L_{\rm bol}$–T relationship with and without point sources

The effect of the point sources on $L_{\rm bol}$–T relation can be evaluated by direct comparison of the relations obtained by including and excluding the point sources. We first analyzed the $L_{\rm bol}$–T using the gas temperature estimated within $R_{\rm spec}$. Then, in order to consider the contribution on the temperature of all the sources within the extended region where the luminosity is computed, we used the gas temperature estimated within $R_{\rm ext}$. We express the $L_{\rm bol}$–T relation as

$$L_{\rm bol,44} = C T_6^{\alpha} \tag{3}$$

where $L_{\rm bol,44}$ is the bolometric luminosity in units of 10^{44} erg s^{-1} and $T_6 = T({\rm keV})/6$.

The data and the fitted $L_{\rm bol}$–T (using a χ^2 method which takes into account the $L_{\rm bol}$ and T uncertainties) are displayed in Fig. 8 for both the $R_{\rm spec}$ (top) and $R_{\rm ext}$ (bottom), and the best-fit parameters are listed in Table 3. Solid and open symbols and solid and dashed lines represent quantities with and without point source inclusion. The most discrepant point in both plots is the cluster ZW CL 1454.8+2233 which was excluded from the fit of the $L_{\rm bol}$–T relation (see Notes on individual clusters in Sect. 4). The inclusion of the point sources, for both $R_{\rm spec}$ and $R_{\rm ext}$, does not have any significant effect on the slope and normalization of the $L_{\rm bol}$–T relation. This is because the correction to T and $L_{\rm bol}$ applied to each data point in the plot produces a shift in the $T - L_{\rm bol}$ plane almost parallel to the best-fit line. In Paper II (Branchesi et al. 2007b) we analyze in more detail the $L_{\rm bol}$–T relation using data free of point sources.

7. Summary and conclusions

In this paper we have presented the details of the data analysis of a sample of 18 distant clusters ($0.25 < z < 1.01$) taken from the *Chandra* archive to derive the observational properties of the X-ray emitting gas. The same sample was used to study the point source counts in the inner region of distant clusters (BR07) and to study the evolution with redshift of the $L_{\rm bol}$–T relation (Branchesi et al. 2007b, Paper II).

The very high angular resolution of *Chandra* that allows to isolate X-ray point sources embedded in the more extended X-ray emission from galaxy clusters, enabled us to estimate for the 18 clusters the effect of the point source non-thermal emission on the determination of the thermal emission due to the cluster itself.

i) The point sources located within the cluster thermal emission region may affect considerably the estimates of X-ray observables like cluster temperature (by an amount up to 13%) and luminosity (by an amount of 17%). These percentages become larger if one considers clusters with $z > 0.7$ where temperature and luminosity increase up to 24% and 22%, respectively (see Sect. 5). The results obtained suggest that, in order to estimate properly the observational parameters of the thermal emission, the point source contribution should be removed.

ii) However, the inclusion (or exclusion) of point sources in the analysis of the $L_{\rm bol}$– T relation, indicates minor differences, within the uncertainties, of the relation (see Sect. 6). This is due to the fact that for each cluster the correction to be applied to T and $L_{\rm bol}$ for the presence of point sources produces a moderate shift in the $L_{\rm bol}$–T plane almost parallel to the best-fit of the "correct" (excluding the point sources) $L_{\rm bol}$–T relation.

Acknowledgements. This research made use of data obtained from the Chandra Data Archive, which is part of the Chandra X-Ray Observatory Science Center,for the National Aeronautics and Space Administration (NASA) by the Smithsonian Astrophysical Observatory. Partial financial support for this work came from the Italian Space Agency ASI (Agenzia Spaziale Italiana) through grant ASI-INAF I/023/05/0.

References

Allen, S. W., Fabian, A. C., Edge, A. C., et al. 1996, MNRAS, 283, 263
Boella, G., Butler, R. C., Perola, G. C., et al. 1997, A&AS, 122, 299
Borgani, S., Rosati, P., Tozzi, P., et al. 2001, ApJ, 561, 13
Branchesi, M., Gioia, I. M., Fanti, C., Fanti, R., & Cappelluti, N. 2007a, A&A, 462, 449 (BR07)
Branchesi, M., Gioia, I. M., Fanti, C., Fanti, R. 2007b, A&A, 472, 739 (Paper II)
Cash, W. 1979, ApJ, 228, 939
Cavaliere, A., & Fusco-Femiano, R. 1976, A&A, 49, 137
Dickey, J. M., & Lockman, F. J. 1990, ARA&A, 28, 215
Donahue, M., Voit, G. M., Gioia, I., et al. 1998, ApJ, 502, 550
Donahue, M., Voit, G. M., Scharf, C. A., et al. 1999, ApJ, 527, 525
Donahue, M., Gaskin, J. A., Patel, S. K., et al. 2003, ApJ, 598, 190
Ettori, S., Tozzi, P., Borgani, S., & Rosati, P. 2004, A&A, 417, 13 (ET04)
Freeman, P. E., Kashyap, V., Rosner, R., & Lamb, D. Q. 2002, ApJS, 138, 185
Frontera, F., Costa, E., dal Fiume, D., et al. 1997, A&AS, 122, 357
Gioia, I. M., Maccacaro, T., Schild, R. E., et al. 1990, ApJS, 72, 567
Gioia, I. M., Braito, V., Branchesi, M., et al. 2004, A&A, 419, 517
Jee, M. J., White, R. L., Ford, H. C., et al. 2005, ApJ, 634, 813
Jeltema, T. E., Canizares, C. R., Bautz, M. W., et al. 2001, ApJ, 562, 124
Kaastra, J. S. 1992, An X-Ray Spectral Code for Optically Thin Plasmas (Internal SRON-Leiden Rep., version 2.0; Leiden: SRON)
Liedahl, D. A., Osterheld, A. L., & Goldstein, W. H. 1995, ApJ, 438, L115
Maughan, B. J., Jones, C., Forman, W., Van Speybroeck, L. 2007 [arXiv:astro-ph/0703156]
Manzo, G., Giarrusso, S., Santangelo, A., et al. 1997, A&AS, 122, 341
Marshall, H. L., et al. 2003, Chandra Calibration Workshop (Cambridge: CXC), http://cxc.harvard.edu/ccw/proceedings/03_proc/presentations/marshall2
Mazzotta, P., Markevitch, M., Forman, W. R, et al. 2001 [arXiv:astro-ph/0108476]
Mushotzky, R. F., & Scharf, C. A. 1997, ApJ, 482, L13
Nousek, J. A., & Shue, D. R. 1989, ApJ, 342, 1207
Parmar, A. N., Martin, D. D. E., Bavdaz, M., et al. 1997, A&AS, 122, 309
Strüder, L., Briel, U., Dennerl, K., et al. 2001, A&A, 365, L18
Tanaka, Y., Inoue, H., & Holt, S. S. 1994, PASJ, 46, L37
Tozzi, P., Rosati, P., Nonino, M., et al. 2001, ApJ, 562, 42
Tozzi, P., Rosati, P., Ettori, S., et al. 2003, ApJ, 593, 705
Trümper, J. 1984, Adv. Space Res., 3, 483
Turner, M. J. L., Abbey, A., Arnaud, M., et al. 2001, A&A, 365, L27
van Speybroeck, L. P., Jerius, D., Edgar, R. J., et al. 1997, Proc. SPIE, 3113, 89
Vikhlinin, A., VanSpeybroeck, L., Markevitch, M., et al. 2002, ApJ, 578, L107 (VI02)
Vikhlinin, A., Markevitch, M., Murray, S. S., et al. 2005, ApJ, 628, 655

Online Material

Appendix A: Analysis of the best-fit parameters

A.1. Comparison between Cash and χ^2 statistics

In this Appendix we compare the best-fit temperatures and the bolometric luminosities obtained with the Cash and the χ^2 statistics only for those spectrum files with the point sources excised. The agreement is remarkably good when the spectra are extracted within the region defined using $R_{\rm spec}$ (see Fig. A.1). The temperatures (luminosities) obtained with the Cash statistics are, on average, ∼1% (∼4%) higher then those obtained with the χ^2 statistics. The histogram of the ratios between the temperatures (luminosities) obtained with the χ^2 and the Cash statistics is characterized by a standard deviation of 0.04 (0.03).

The agreement remains good considering the more extended region defined when one uses the radius $R_{\rm ext}$. In this case the luminosities with the Cash statistics are on average ∼3% smaller than those obtained with χ^2, while the temperatures remain the same. The dispersion of the temperature histogram obtained within the region defined by $R_{\rm ext}$ has a standard deviation of 0.1, higher than the dispersion obtained when using $R_{\rm spec}$. This is presumably due to the fact that the spectral fit is better in the region that optimizes the signal to noise ratio.

A.2. Best parameters for luminosity and temperature

The quality of the fits is better inside the region within $R_{\rm spec}$, e.g. the region that maximizes the signal to noise ratio. Thus the temperatures estimated within this region, $T_{R_{\rm spec}}$, are considered more representative of the actual average temperature of the gas. On the other hand the cluster luminosities are estimated within the extended region defined by the radius $R_{\rm ext}$ in order to take into account the faint brightness tails at the cluster boundaries as well as the point sources in those regions. For each cluster the luminosity was calculated by fitting the counts accumulated within $R_{\rm ext}$ with a thermal bremsstrahlung model. A best-fit temperature, indicated as $T_{R_{\rm ext}}$, is associated to each thermal model. Systematic differences between $T_{R_{\rm spec}}$ and $T_{R_{\rm ext}}$ are within 3%.

In order to understand how strongly the luminosity depends on the model and on its associated temperature, and in order to know which errors are involved when temperature and luminosity are calculated in two different regions (i.e. defined by $R_{\rm spec}$ and R_{ext}, respectively) we computed the luminosity of each cluster in the $R_{\rm ext}$ region but using the temperature obtained within $R_{\rm spec}$. The results of this exercise are shown in Fig. A.2. The two methods give values consistent within the errors. The differences between the luminosities are all within 5%, that is within the statistical errors.

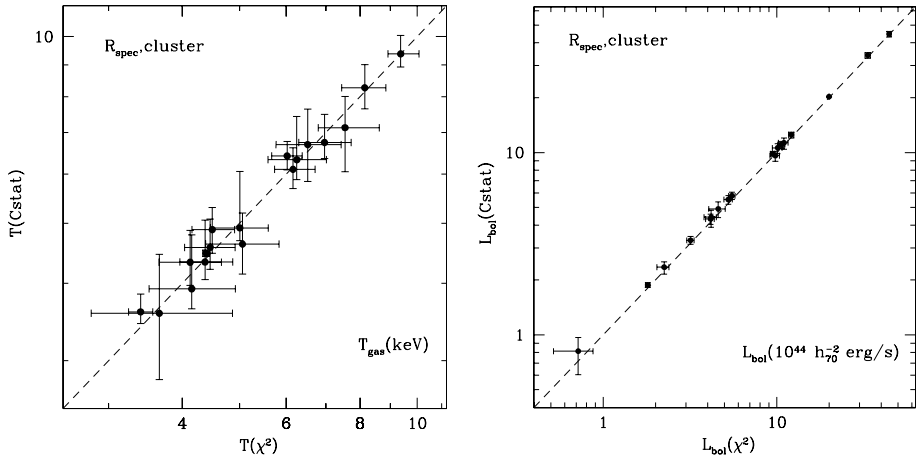

Fig. A.1. (*Left panel*) The best-fit temperature obtained using the Cash statistics versus the best-fit temperature obtained with the χ^2 statistics. The dashed line is equality between the two temperatures. (*Right panel*) The luminosity obtained using the Cash statistics versus the best-fit luminosity obtained using the χ^2 statistics. The dashed line is equality between the two luminosities.

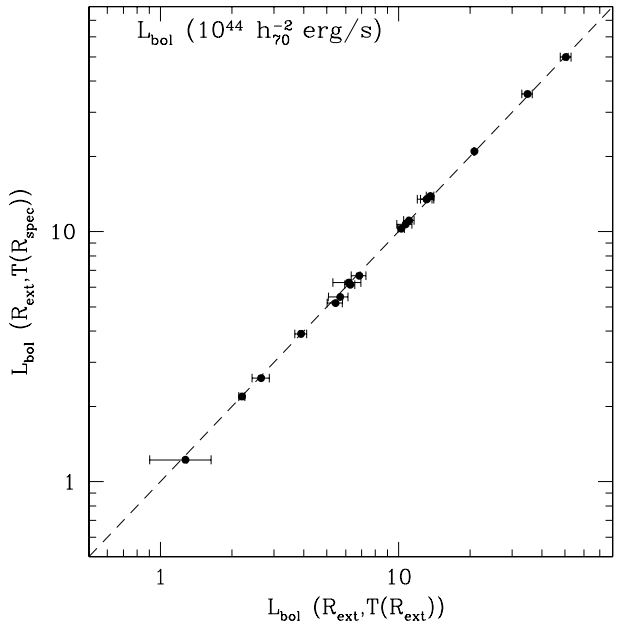

Fig. A.2. Best-fit luminosity obtained within $R_{\rm ext}$ with the temperature fixed to the value obtained within $R_{\rm spec}$ versus best-fit luminosity obtained within $R_{\rm ext}$. The dashed line is equality between the two best-fit luminosities.